ARTICLE   **OPEN**

Observation of Bloch oscillations and Wannier-Stark localization on a superconducting quantum processor

Xue-Yi Guo[1,7], Zi-Yong Ge[1,2,7], Hekang Li[1,2], Zhan Wang[1,2], Yu-Ran Zhang[3], Pengtao Song[1,2], Zhongcheng Xiang[1], Xiaohui Song[1], Yirong Jin[4], Li Lu[1,2,5,6], Kai Xu[1,5], Dongning Zheng[1,2,5,6 ✉] and Heng Fan[1,2,5,6 ✉]

The Bloch oscillation (BO) and Wannier-Stark localization (WSL) are fundamental concepts about metal-insulator transitions in condensed matter physics. These phenomena have also been observed in semiconductor superlattices and simulated in platforms such as photonic waveguide arrays and cold atoms. Here, we report experimental investigation of BOs and WSL simulated with a 5-qubit programmable superconducting processor, of which the effective Hamiltonian is an isotropic XY spin chain. When applying a linear potential to the system by properly tuning all individual qubits, we observe that the propagation of a single spin on the chain is suppressed. It tends to oscillate near the neighborhood of their initial positions, which demonstrates the characteristics of BOs and WSL. We verify that the WSL length is inversely correlated to the potential gradient. Benefiting from the precise single-shot simultaneous readout of all qubits in our experiments, we can also investigate the thermal transport, which requires the joint measurement of more than one qubits. The experimental results show that, as an essential characteristic for BOs and WSL, the thermal transport is also blocked under a linear potential. Our experiment would be scalable to more superconducting qubits for simulating various of out-of-equilibrium problems in quantum many-body systems.

INTRODUCTION

The transport phenomena in solids is one of the central topics in condensed matter physics. About 80 years ago, Bloch and Zener predicted that electrons cannot spread uniformly in a crystal lattice under a constant force, and instead, they would oscillate and localize[1–3]. This oscillation is called Bloch oscillations (BOs), and the corresponding localization is called Wannier-Stark localization (WSL). BOs and WSL are typical quantum effects which reveal the wave properties of electrons. However, they can hardly be observed directly in normal bulk materials due to the requirement of long coherence times. It is not until the 1990s that these phenomena were observed experimentally in semiconductor superlattices[4]. Nevertheless, the relaxation time in this type of material is still a bottleneck for studying BOs and WSL. During the last two decades, the developments in quantum technology have made it possible to simulate these quantum phenomena in artificial quantum systems[5,6]. Compared with the semiconductor superlattice systems, these artificial quantum systems have much longer decoherence times making them suitable for the experimental study of BOs. BOs in bosonic systems have been observed in the cold atoms[7–16] and photonic waveguide arrays[17], etc.

Due to the scalability, long decoherence time and high-precision control, the superconducting circuit[18,19] has become a competitive candidate for achieving universal quantum computation and have demonstrated quantum supremacy[20]. Superconducting circuits can be fabricated into different lattice structures, such as 1D chain, ladder, fully connected graphs, and 2D square lattice. It is a versatile platform for performing various kinds of quantum-simulation experiments, e.g., quantum many-body dynamics[21–34], quantum chemistry[35,36], and implementing quantum algorithms[37–42]. Our quantum processor with 1D array of

superconducting qubits is well suited for studying essential transport properties of spin and energy in BOs and WSL. Remarkably, measurements of energy transport are absent in previous simulations, which needs capability of multiqubits single-shot simultaneous readout in obtaining nearest-neighbor two-site correlations.

In this work, we experimentally investigate BOs and WSL of spin system on a 5-qubit superconducting processor. The effective Hamiltonian can be described by an isotropic XY chain. By manipulating the frequencies of superconducting qubits precisely, we can construct a linear potential. Under this type of potential, we observe that the spin can hardly propagate through the lattice during the quench dynamics. It tends to oscillate at the vicinity of initial positions, which is a typical phenomenon of BOs and WSL. In addition, using the maximum probability of a photon propagating from one boundary to another to represent the WSL length, we can demonstrate that the localization length is inversely correlated to the potential gradient. By performing precise simultaneous readout of two superconducting qubits, we can also study the thermal transport of the system. It is shown that the energy transport is suppressed as well by the linear potential.

RESULTS
Experimental setup and model

In this experiment, our superconducting processor contains 5 qubits arranged into a 1D chain, with the capability of high-precision simultaneous readouts and full controls, see Fig. 1(a). The Hamiltonian of the system can be described by the 1D

---

[1]Beijing National Laboratory for Condensed Matter Physics, Institute of Physics, Chinese Academy of Sciences, Beijing, China. [2]School of Physical Sciences, University of Chinese Academy of Sciences, Beijing, China. [3]Theoretical Quantum Physics Laboratory, RIKEN Cluster for Pioneering Research, Wako-shi, Saitama, Japan. [4]Beijing Academy of Quantum Information Sciences, Beijing, China. [5]CAS Center for Excellence in Topological Quantum Computation, UCAS, Beijing, China. [6]Songshan Lake Materials Laboratory, Dongguan, China. [7]These authors contributed equally: Xue-Yi Guo, Zi-Yong Ge. ✉email: dzheng@iphy.ac.cn; hfan@iphy.ac.cn

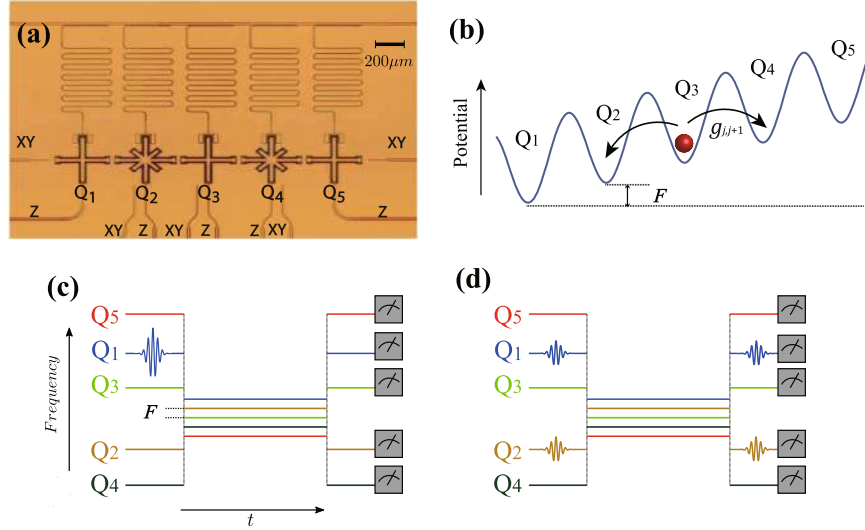**Fig. 1 Experimental setup. a** Circuit diagram of the device. There are 5 superconducting transmon qubits ($Q_1 - Q_5$) arranged into a chain[47–52]. The nearest-neighbor two qubits are coupled capacitively, and the negative anharmonicity U of each qubit gives the on-site attractive interaction. The frequency of each qubit is tunable by individual microwave driving through the flux-bias line (Z line). The qubit flipping can be realized by XY lines. Each qubit is coupled to a resonator for individual and simultaneous readout. More experimental details of the system are presented in the Supplementary Note 1. **b** The sketch of the corresponding Bose-Hubbard chain with a linear potential. The detuning of the nearest-neighbor two qubits is the potential gradient F. The red ball represents the photon (the excitation of the qubit), which can tunnel to the nearest-neighbor sites (black arrows). **c** Pulse sequences for studying the transport of spin. The qubits are ordered by their frequencies, and initialized at their idle frequencies and the state $|0\rangle$, see Supplementary Note 1. A. Then, we excite Q_1 to the state $|1\rangle$ by a X gate and bias all qubits at the work point with square waves. After the system evolves for a specific time t, all qubits are biased back to their idle frequencies, and we finally read out each qubit. **d** Pulse sequences for studying the thermal transport. We use two $X/2$ gates at Q_1 and Q_2 two prepare the initial state $|X_+X_+000\rangle$, and other sequences is the same as **c**.

Bose-Hubbard model, which reads ($\hbar = 1$)[24,31,32]

$$\hat{H} = \sum_{j=1}^{4} g_{j,j+1}(\hat{a}_j^\dagger \hat{a}_{j+1} + \hat{a}_{j+1}^\dagger \hat{a}_j) + \sum_{j=1}^{5}\left(\frac{U_j}{2}\hat{n}_j(\hat{n}_j - 1) + h_j\hat{n}_j\right), \quad (1)$$

where $\hat{a}_j^\dagger$ ($\hat{a}_j$) is the photon creation (annihilation) operator, $\hat{n}_j \equiv \hat{a}_j^\dagger \hat{a}_j$ is the number operator, $g_{j,j+1}$ is the nearest-neighbor coupling strength, $U_j < 0$ is the on-site attractive interaction resulted from the anharmonicity, and h_j is the local potential which is tunable by DC biases through Z lines. To realize BOs, we let h_j vary linearly along the lattice sites, i.e., $h_j = Fj$, where F is the potential gradient or the detuning of nearest-neighbor two qubits, see Fig. 1(b).

In this superconducting circuits, since $|U_j|/g_{i,j} \gg 1$ and U_j is staggered to suppress higher order tunneling (see Supplementary Note 1. A), the Fock space of the photons at each qubit can be truncated to two dimensions. Thus, the model is equivalent to a spin-$\frac{1}{2}$ system, and the nonlinear term can be neglected. Therefore, the effective Hamiltonian of Eq. (1) can be reduced to an isotropic XY model[31,32]

$$\hat{H}_{\text{eff}} = \sum_{j=1}^{4} g_{j,j+1}(\hat{\sigma}_j^+ \hat{\sigma}_{j+1}^- + \hat{\sigma}_{j+1}^+ \hat{\sigma}_j^-) + \sum_{j=1}^{5} h_j \hat{\sigma}_j^+ \hat{\sigma}_j^-, \quad (2)$$

where $\hat{\sigma}^\pm = (\hat{\sigma}^x \pm i\hat{\sigma}^y)/2$, and $\hat{\sigma}^{x,y,z}$ are Pauli matrices. According to Eqs. ((1)–(2)), we know that the system has an $U(1)$ symmetry, so that the total spins $\sum_{j=1}^{5} \hat{\sigma}_j^+ \hat{\sigma}_j^-$ for $\hat{H}_{\text{eff}}$ (or the total photon number $\sum_{j=1}^{5} \hat{n}_j$ for $\hat{H}$) are conserved. In the following discussion, we do not distinguish the photons and spins. In addition, this system is time-independent, thus the energy is also conserved, where we can explore both spin and thermal transport in this system. Note that we only consider the evolution time $t \leq 300$ ns in the experiment, which is much smaller than decoherence time (more than 17 μs, see Supplementary Note 1. A). Therefore, the above conservation laws are nearly unbroken under the impact of decoherence.

Spin transport

Firstly, we study the spin transport after a quantum quench. The explicit experiment sequences are shown in Fig. 1(c). We initially excite the leftmost qubit Q_1 from the state $|0\rangle$ to $|1\rangle$ by a X gate, i.e., the initial state is $|\psi(0)\rangle = |10000\rangle$. Then, each qubit is biased to the working frequency with the fast Z pulse, and the system will evolve under the Hamiltonian (2). Finally, we measure, for each qubit, the probability distribution of state $|1\rangle$, i.e., the density distribution of the photon or spin, defined as

$$P_j(t) := \langle\psi(t)|\hat{\sigma}_j^+ \hat{\sigma}_j^-|\psi(t)\rangle, \quad (3)$$

where $|\psi(t)\rangle = e^{-i\hat{H}t}|\psi(0)\rangle$ is the wave function of the system at time t. As shown in Fig. 2(a), when $F = 0$, the spin displays a light-cone-like propagation without any restrictions and can exhibit a reflection when approaching the boundaries[31,32]. Nevertheless, according to Fig. 2(b–d), when $F \neq 0$, the spin transport is blocked. With an increase of $|F|$, the spin can hardly propagate from the leftmost to the rightmost. Instead, it tends to oscillate around the neighbor of the initial position, and this is a typical signature of BOs and WSL. In Fig. 2(e–h), we present the corresponding numerical results, which are consistent with the experimental results. From Fig. 2(d), we can know that the BO frequency is about 50 ns when $F/2\pi = 15$ MHz, which is much smaller than the decoherence time of the superconducting qubits.

Now we extract the oscillation amplitude or WSL length ξ_{WS}. Generally, in the presence of linear potential, the single-particle wave function is localized and has the form $\psi(x) \sim Ae^{-x/\xi_{WS}}$, where A is a normalized factor. Hence, the probability that a particle can propagate the distance r, i.e., $P(r)$, should satisfy $P(r) \propto e^{-r/\xi_{WS}}$. In this experiment, the existence of boundaries makes it challenging to obtain the localization length. To overcome this difficulty, we propose another method to extract the WSL length. With the maximum photon occupancy probabilities at Q_5, defined as $P_5^{\text{max}} := \max_{t>0} P_5(t)$, we can obtain the WSL length using $\xi_{WS} \propto 1/\ln P_5^{\text{max}}$. In Supplementary Note 2, we present a phenomenological proving of this relation. To extract
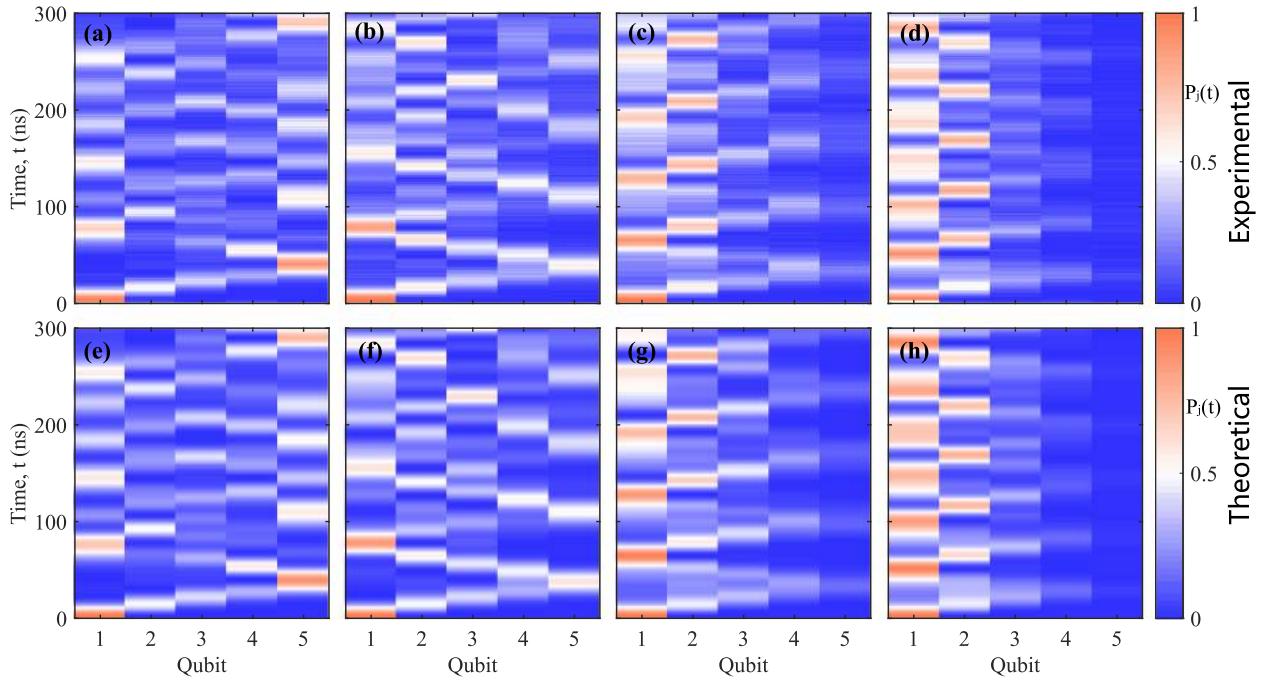
Fig. 2   Spin transport. The experimental results for the time evolution of density distribution $P_j(t)$ up to 300 ns. The initial state is $|10000\rangle$, and the potential gradient (**a**) $F/2\pi = 0$, (**b**) $F/2\pi = 5$, (**c**) $F/2\pi = 10$, (**d**) $F/2\pi = 15$ MHz. The photon or the spin can exhibit a light-cone-like spreading in the system. As the increase of F, the photon becomes more difficult to propagate to the right boundary, instead, it tends to oscillate in the vicinity of the initial position. Each point shows the average of 6×100 single-shot measurements. **e–h** The corresponding theoretical results of **a–d**. The numerical and experimental results are consistent with each other. The details of numerical method are presented in "Methods".

more reliable P_5^{max}, we use Gaussian function to fit $P_5(t)$ and take the corresponding peak value as P_5^{max}, see Fig. 3(a). Now we study the relation between the potential gradient F and P_5^{max}. For a WSL system, the localization length ξ_{WS} is inversely proportional to F, i.e., $\xi_{WS} \propto 1/F$. Hence, we expect that $\ln P_5^{max} \propto F$. According to Fig. 3(b), we can find that both the numerical simulation and experimental results are consistence with this relation.

Thermal transport

Now we focus on the thermal transport in this system. For a 1D chain, the energy density at the j-th bond is defined as $\hat{\rho}_j^E = \hat{H}_{j,j+1} \equiv \hat{\rho}_j^K + \hat{\rho}_j^P$, where $\hat{\rho}_j^K$ and $\hat{\rho}_j^P$ denote kinetic energy and potential energy densities, respectively. From Eq. (2), these two quantities can be expressed as

$$\begin{aligned} \hat{\rho}_j^K &= \tfrac{1}{2} g_{j,j+1} (\hat{\sigma}_j^x \hat{\sigma}_{j+1}^x + \hat{\sigma}_j^y \hat{\sigma}_{j+1}^y), \\ \hat{\rho}_j^P &= h_n \hat{\sigma}_j^+ \hat{\sigma}_j^- + h_{j+1} \hat{\sigma}_{j+1}^+ \hat{\sigma}_{j+1}^-. \end{aligned} \quad (4)$$

In general, the thermal transport is closely related to the electronic charge transport in a classical metal system, which is known as the Wiedemann-Franz [43,44] law, i.e., $\lambda/\sigma = LT$, where λ is thermal conductance, σ is electronic conductance, T is temperature, and L is Lorenz number. Eq. (5) shows that the potential energy only depends on the spin distribution, which displays BOs and WSL as discussed in the previous section. Here, we consider the time evolution of the kinetic energy density.

In Fig. 1(d), the pulse sequences of this experiment are presented. To study the transport of $\hat{\rho}_j^K$, the kinetic energy densities should exist a gradient between two edges at the initial state. Here, we choose the initial state as $|X_+X_+000\rangle$, where $|X_+\rangle = \frac{1}{\sqrt{2}}(|0\rangle + |1\rangle)$ is the eigenstate of $\hat{\sigma}^x$ with eigenvalue 1 and can be prepared by $X/2$ gate. We can verify that, with this initial state, the kinetic energy at left edge is larger than one at right edge, so this initial state can be used to study the thermal transport. Then, $\langle \hat{\rho}_1^K(t) \rangle$ and $\langle \hat{\rho}_4^K(t) \rangle$, i.e., the kinetic energy

densities of two edges, are measured, where the simultaneous readout of the nearest-neighbor two qubits is necessary. As shown in Fig. 4(a), when $F = 0$, the kinetic energies of two edges can exchange almost freely. Nevertheless, from Fig. 4(b), we can find that the difference between $\langle \hat{\rho}_1^K(t) \rangle$ and $\langle \hat{\rho}_4^K(t) \rangle$ always exist, when $F/2\pi = 15$ MHz. Therefore, similar to the spins, the thermal transport is also suppressed under the linear potential.

Due to the $U(1)$ symmetry, the quench dynamics can be decomposed into different particle-number subspace, and different subspaces are decoupled with each other. For the initial state $|X_+X_+000\rangle$, the photons only bunch at Q_1 or Q_2. Despite existence of two-excitation populating for this initial state, Hamiltonian (2) can still effectively describe the dynamics of this system, since two excitations can hardly bunch at a same site due to large and staggered U_j. Thus, we can use Slater determinant to calculate the dynamics of two-excitation sector. We can verify that the spins are localized among all of these subspaces with $F \neq 0$. The spins can hardly propagate to the other side, so Q_4 and Q_5 almost remain at the initial state $|00\rangle$. Therefore, the change of $\langle \hat{\rho}_4^K \rangle$ is small in this case, i.e., the kinetic energy can hardly transport from the left edge to the right edge. In this picture, we can know that the restriction of energy transport origins from the localization of the spins, which is identified with the classical Wiedemann-Franz law.

DISCUSSION

In summary, we have reported the experimental observation of BOs and WSL on a 5-qubit superconducting processor. We provide another representation of the WSL length for a finite size system, i.e., the probability that a photon can propagate from one edge to anther edge. Using this representation, we verify that the WSL length is inversely proportional to the potential gradients. Furthermore, benefiting from the precise simultaneous readout of two qubits, the thermal transport in this system is also studied. The evolution of the energy densities shows that the thermal
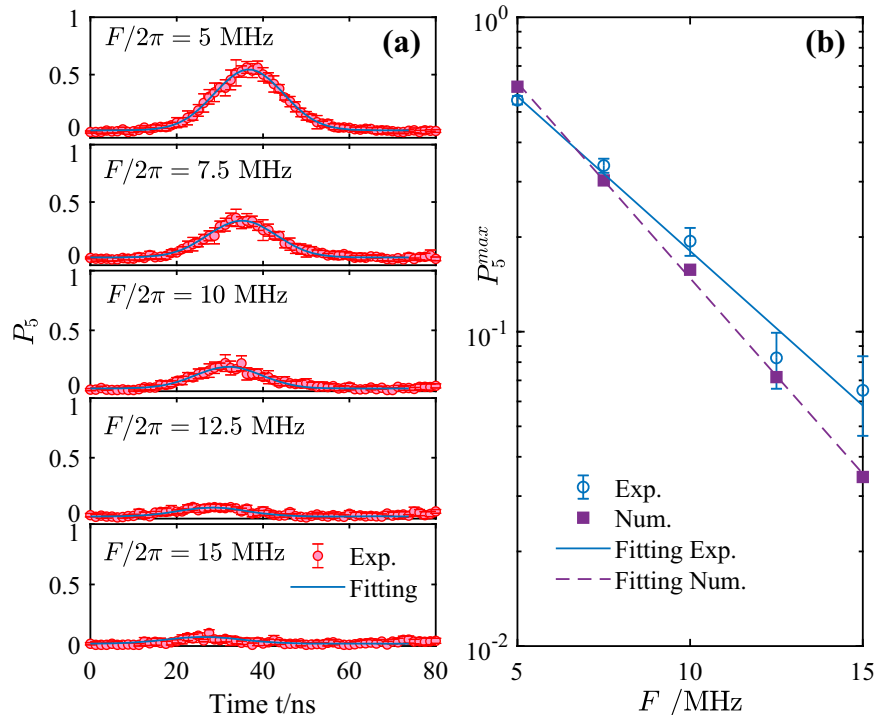
Fig. 3 Extracting WSL length. a The time evolution of photon occupancy probabilities at Q_5 for different potential gradients F. The initial state is $|10000\rangle$. The red solid circles are experimental data points, and the blue lines are Gaussian fittings. The estimate method of errors is presented in "Methods". **b** The relation between P_5^{max} and F, where the experimental P_5^{max} is the peak value of Gaussian curve shown in **a**. The corresponding error bars are the fitting errors. The numerical data points are peak values of the first wavefronts of $P_5(t)$ without Gaussian fitting[31]. Here, $\ln P_5^{max}$ is nearly linearly related to the potential gradients F. The solid and dashed lines are the corresponding linear fittings of the experimental and theoretic results, respectively.

transport, akin to the spins, is not free under the linear potential, neither.

Comparing to the other artificial quantum many-body systems, one of the most significant advantages of the superconducting quantum circuits is that the states of superconducting qubits can be measured in an arbitrary basis. Thus, it enables us to study the thermal transport associated with BOs, which is generally a challenge for other platforms. Our results reveal that the superconducting quantum circuits can be considered as alternative synthetic quantum systems for experimentally exploring BOs and other quantum physics. Our platform may be useful for the further study of BOs, such as studying the BO frequency and spin current (see Supplementary Note 3), and imaging the Bloch band through BOs[16]. Our platform can also be extended to studying the transport phenomenon in other specific systems, for instance, in the presence of disorder potentials or engineered noises. In addition, it is meaningful to extend this system to the interacting case, and the Stark many-body localization may be realized in this system[45,46]. To explore these problems, our system could be scaled to include more qubits with longer decoherence time.

METHODS
Setup
This 5-qubit device is made in the following processes: (i) Depositing Aluminum. A 100-nm-thick Al layer is deposited on a 10×10 mm c-plane sapphire substrate by means of electron-beam evaporation with a base pressure lower than 10^{-9} Torr. (ii) Etching the wires, resonators, and capacitor. We use a direct laser writer (DWL66+) and wet etching to produce microwave coplanar waveguide resonators, transmission lines, control lines, and capacitors of the Xmon qubit. The resist used here is S1813, and wet-etching process is carried out with Aluminum Etchant Type A. (iii) Fabricating Josephson junctions. The Josephson junctions of qubits are fabricated by the double-angle evaporation process. In this step, the

undercut structure is made by a PMMA-MMA double layer EBL resist following the process similar to one reported in ref.[47]. During the evaporation, the bottom electrode is about 30 nm thick, while the top electrode is about 100 nm thick with intermediate oxidation.

We package the device in an aluminum alloy sample box and fix the box on the mixing chamber stage of a dilution refrigerator. The temperature of the mixing chamber is below 15 mK during measurements. In order to reduce the external electromagnetic interference, an aluminum can and a μ-metal can are placed outside the sample box.

For each qubit, microwave pulses are applied through XY lines to rotate the qubit state between $|0\rangle$ and $|1\rangle$. Such XY pulses are formed by modulating continuous microwave signals sent from arbitrary waveform generators (AWGs: Zurich instruments HDAWG) via IQ mixers. To control all 5 qubits, the signal from a microwave source is divided into 5 channels through a power splitter, and each channel is amplified by a 11 dBm level. Current pulses are applied through Z control lines to tune the qubit frequencies. We use a DC current source (Yokogawa GS220) to apply static direct current to bias a qubit to its idle frequency and use an AWG to apply a fast current pulse to tune the qubit frequencies dynamically. Such static direct current and fast current pulses are combined by a bias-Tee, of which the capacitor is removed.

Readout pulses are composed of five tones at 40-MHz intervals. Each pulse corresponds to one qubit and is applied through the readout line. The output signals are amplified by a broad band Josephson parametric amplifier (JPA)[48] and a low temperature HEMT amplifier before further enhancement by a room temperature amplifier. The amplified signal is demodulated by a IQ Mixer and acquired by an analog-digital converter (ADC: Alazar ATS9360).

Attenuators, filters and isolators are used to reduce and isolate the noise from the electronic instruments, active electronic components (such as JPA and HEMT) and passive components outside the mixing chamber.

Error estimation
In our experiments, for the single-qubit readout, e.g., Fig. 3(a), each point shows the average of 6×100 single-shot measurements. To estimate the errors, we equally divide these single-shot readout data into 6 groups (each group contains 100 readouts). Thus, we can obtain 6 expectation
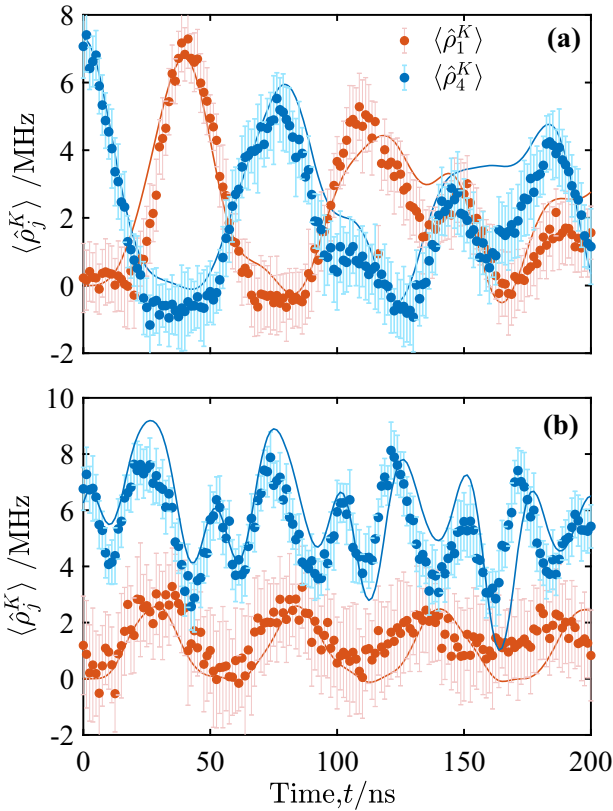
Fig. 4 Time evolution of kinetic energy densities at two edges, i.e., $\langle \hat{\rho}_1^K(t) \rangle$ and $\langle \hat{\rho}_4^K(t) \rangle$. Symbols are experimental data points, and the solid lines represent numerical results, where the decoherence and dephase are considered. The initial state is $|X_+X_+000\rangle$. Each point shows the average of 10×200 single-shot measurements, and the estimate method of errors is presented in "Methods". **a** $F/2\pi = 0$ MHz. The energy densities $\langle \hat{\rho}_1^K \rangle$ and $\langle \hat{\rho}_4^K \rangle$ can almost exchange into each other indicating that the energy transport is free in this case. **b** $F/2\pi = 15$ MHz. There is no crossing between the curves $\langle \hat{\rho}_1^K(t) \rangle$ and $\langle \hat{\rho}_4^K(t) \rangle$. The existence of this energy gradient between two edges shows that the energy transport is compressed. That is, the energies at one side can hardly spread to the other side.

values for each point, and the error bar is the standard deviation of these 6 expectation values. For the two-qubit readout, e.g., Fig. 4, each point shows the average of 10×200 single-shot measurements. We use the same method to estimate the errors, where the readout data are equally divided into 10 groups.

Numerical methods
The numerical results are obtained by numerically solving the Lindblad master equation, which reads

$$
\begin{aligned}
\frac{d}{dt}\rho(\hat{t}) =\ & -i[\hat{H}, \rho(\hat{t})] \\
& + \frac{1}{2}\sum_{n=1}^{5}\left[2\hat{\Gamma}_n\rho(\hat{t})\hat{\Gamma}_n^\dagger - \rho(\hat{t})\hat{\Gamma}_n\hat{\Gamma}_n^\dagger - \hat{\Gamma}_n\hat{\Gamma}_n^\dagger\rho(\hat{t})\right] \\
& + \frac{1}{2}\sum_{n=1}^{5}\left[2\hat{A}_n\rho(\hat{t})\hat{A}_n^\dagger - \rho(\hat{t})\hat{A}_n\hat{A}_n^\dagger - \hat{A}_n\hat{A}_n^\dagger\rho(\hat{t})\right],
\end{aligned}
\tag{5}
$$

where $\rho(\hat{t})$ is the density matrix at time t, and Lindblad operators $\hat{\Gamma}_n = \sqrt{1/\mathcal{T}_1}\hat{a}_n$ and $\hat{A}_n = \sqrt{1/\mathcal{T}_2^*}\hat{a}_n^\dagger\hat{a}_n$ represent the excitation leakage and dephasing, respectively. The corresponding parameters applied here have been calibrated experimentally, and the details are shown in Supplementary Note 1. A.

REFERENCES
1. Bloch, F. Über die quantenmechanik der elektronen in kristallgittern. *Z. Phys.* **52**, 555 (1929).
2. Zener, C. A theory of the electrical breakdown of solid dielectrics. *Proc. R. Soc. A* **145**, 523 (1934).
3. Wannier, G. H. Dynamics of band electrons in electric and magnetic fields. *Rev. Mod. Phys.* **34**, 645 (1962).
4. Feldmann, J. Optical investigation of Bloch oscillations in a semiconductor superlattice. *Phys. Rev. B* **46**, 7252 (1992).
5. Buluta, I. & Nori, F. Quantum simulators. *Science* **326**, 108 (2009).
6. Georgescu, I. M., Ashhab, S. & Nori, F. Quantum simulation. *Rev. Mod. Phys.* **86**, 153 (2014).
7. Ben Dahan, M., Peik, E., Reichel, J., Castin, Y. & Salomon, C. Bloch oscillations of atoms in an optical potential. *Phys. Rev. Lett.* **76**, 4508 (1996).
8. Anderson, B. P. & Kasevich, M. A. Macroscopic quantum interference from atomic tunnel arrays. *Science* **282**, 1686 (1998).
9. Morsch, O., Müller, J. H., Cristiani, M., Ciampini, D. & Arimondo, E. Bloch oscillations and mean-field effects of Bose-Einstein condensates in 1D optical lattices. *Phys. Rev. Lett.* **87**, 140402 (2001).
10. Fattori, M. Atom interferometry with a weakly interacting Bose-Einstein condensate. *Phys. Rev. Lett.* **100**, 080405 (2008).
11. Gustavsson, M., Haller, E., Mark, M. J., Danzl, J. G., Rojas-Kopeinig, G. & Nagerl, H. C. Control of interaction-induced dephasing of Bloch oscillations. *Phys. Rev. Lett.* **100**, 080404 (2008).
12. Alberti, A., Ivanov, V. V., Tino, G. M. & Ferrari, G. Engineering the quantum transport of atomic wavefunctions over macroscopic distances. *Nat. Phys.* **5**, 547 (2009).
13. Haller, E. et al. Inducing transport in a dissipation-free lattice with super Bloch oscillations. *Phys. Rev. Lett.* **104**, 200403 (2010).
14. Meinert, F. et al. Interaction-induced quantum phase revivals and evidence for the transition to the quantum chaotic regime in 1D atomic Bloch oscillations. *Phys. Rev. Lett.* **112**, 193003 (2014).
15. Preiss, P. M. et al. Strongly correlated quantum walks in optical lattices. *Science* **347**, 1229 (2015).
16. Geiger, Z. A. et al. Observation and uses of position-space Bloch oscillations in an ultracold gas. *Phys. Rev. Lett.* **120**, 213201 (2018).
17. Morandotti, R., Peschel, U., Aitchison, J. S., Eisenberg, H. S. & Silberberg, Y. Experimental observation of linear and nonlinear optical Bloch oscillations. *Phys. Rev. Lett.* **83**, 4756 (1999).
18. Makhlin, Y., Schön, G. & Shnirman, A. *Rev. Mod. Phys.* **73**, 357 (2001).
19. Gu, X., Kockum, A. F., Miranowicz, A., Liu, Y. & Nori, F. Microwave photonics with superconducting quantum circuits. *Phys. Rep.* **718**, 1 (2017).
20. Arute, F. et al. Quantum supremacy using a programmable superconducting processor. *Nature (London)* **574**, 505 (2019).
21. Eisert, J., Friesdorf, M. & Gogolin, C. Quantum many-body systems out of equilibrium. *Nat. Phys.* **11**, 124 (2015).
22. Braumüller, J. et al. Experimentally simulating the dynamics of quantum light and matter at deep-strong coupling. *Nat. Commun.* **8**, 779 (2017).
23. Xu, K. et al. Emulating many-body localization with a superconducting quantum processor. *Phys. Rev. Lett.* **120**, 050507 (2018).
24. Roushan, P. et al. Spectroscopic signatures of localization with interacting photons in superconducting qubits. *Science* **358**, 1175 (2017).
25. Salathé, Y. et al. Digital quantum simulation of spin models with circuit quantum electrodynamics. *Phys. Rev. X* **5**, 021027 (2015).
26. Barends, R. et al. Digital quantum simulation of fermionic models with a superconducting circuit. *Nat. Commun.* **6**, 7654 (2015).
27. Zhong, Y. P. et al. Emulating anyonic fractional statistical behavior in a superconducting quantum circuit. *Phys. Rev. Lett.* **117**, 110501 (2016).
28. Song, C. et al. Demonstration of topological robustness of anyonic braiding statistics with a superconducting quantum circuit. *Phys. Rev. Lett.* **121**, 030502 (2018).
29. Flurin, E. et al. Observing topological invariants using quantum walks in superconducting circuits. *Phys. Rev. X* **7**, 031023 (2017).
30. Ma, R. et al. A dissipatively stabilized Mott insulator of photons. *Nature* **566**, 51 (2019).

31. Yan, Z. et al. Strongly correlated quantum walks with a 12-qubit superconducting processor. *Science* **364**, 753 (2019).
32. Ye, Y. et al. Propagation and localization of collective excitations on a 24-Qubit superconducting processor. *Phys. Rev. Lett.* **123**, 050502 (2019).
33. Guo, X.-Y. et al. Observation of a dynamical quantum phase transition by a superconducting qubit simulation. *Phys. Rev. Appl.* **11**, 044080 (2019).
34. Xu, K. et al. Probing dynamical phase transitions with a superconducting quantum simulator. *Sci. Adv.* **6**, eaba4935 (2020).
35. O'Malley, P. J. J. et al. Scalable quantum simulation of molecular energies. *Phys. Rev. X* **6**, 031007 (2016).
36. Kandala, A. et al. Hardware-efficient variational quantum eigensolver for small molecules and quantum magnets. *Nature* **549**, 242 (2017).
37. Lucero, E. et al. Computing prime factors with a Josephson phase qubit quantum processor. *Nat. Phys.* **8**, 719 (2012).
38. Gong, M. et al. Genuine 12-Qubit entanglement on a superconducting quantum processor. *Phys. Rev. Lett.* **122**, 110501 (2019).
39. Barends, R. et al. Digitized adiabatic quantum computing with a superconducting circuit. *Nature* **534**, 222 (2016).
40. Zheng, Y. et al. Solving systems of linear equations with a superconducting quantum processor. *Phys. Rev. Lett.* **118**, 210504 (2017).
41. Song, C. et al. 10-qubit entanglement and parallel logic operations with a superconducting circuit. *Phys. Rev. Lett.* **119**, 180511 (2017).
42. Song, C. et al. Observation of multi-component atomic Schrödinger cat states of up to 20 qubits. *Science* **365**, 574 (2019).
43. Franz, R. & Wiedemann, G. Ueber die Wärme-Leitungsfähigkeit der Metalle. *Annalen der Physik* **165**, 497 (1853).
44. Chester, G. & Thellung, A. The Law of Wiedemann and Franz. *Proc. Phys. Soc.* **77**, 1005 (1961).
45. Schulz, M., Hooley, C. A., Moessner, R. & Pollmann, F. Stark many-body localization. *Phys. Rev. Lett.* **122**, 040606 (2019).
46. van Nieuwenburga, E., Bauma, Y. & Refael, G. From Bloch oscillations to many-body localization in clean interacting systems. *Proc. Natl. Acad. Sci. USA* **116**, 9269 (2019).
47. Barends, R. et al. Coherent Josephson qubit suitable for scalable quantum integrated circuits. *Phys. Rev. Lett.* **111**, 080502 (2013).
48. Mutus, J. Y. et al. Strong environmental coupling in a Josephson parametric amplifier. *Appl. Phys. Lett.* **104**, 263513 (2014).
49. You, J. Q., Hu, X., Ashhab, S. & Nori, F. Low-decoherence flux qubit. *Phys. Rev. B* **75**, 140515 (2007).
50. Koch, J. et al. Charge-insensitive qubit design derived from the Cooper pair box. *Phys. Rev. A* **76**, 042319 (2007).
51. Barends, R. et al. Superconducting quantum circuits at the surface code threshold for fault tolerance. *Nature* **508**, 500 (2014).
52. Lucero, E. et al. Reduced phase error through optimized control of a superconducting qubit. *Phys. Rev. A* **82**, 042339 (2010).

AUTHOR CONTRIBUTIONS

Z.Y.G., H.F. and D.Z. conceived the idea, X.Y.G. performed the experiments with assistances from Z.W., P.T.S. and K.X., H.K.L. fabricated the device with assistances from Z.C.X., X.H. S., L.L. and Y.R.J., Z.Y.G. performed the calculations with the help of Y.R.Z., X.Y.G., Z.Y.G., H.F. and D.Z. co-wrote the paper with comments from all co-authors.

COMPETING INTERESTS

The authors declare no competing interests.

ADDITIONAL INFORMATION

Supplementary information The online version contains supplementary material available at https://doi.org/10.1038/s41534-021-00385-3.

Correspondence and requests for materials should be addressed to D.Z. or H.F.

Reprints and permission information is available at http://www.nature.com/reprints

Publisher's note Springer Nature remains neutral with regard to jurisdictional claims in published maps and institutional affiliations.